Structural and Electrical Investigation of C_{60}–Graphene Vertical Heterostructures

Kwanpyo Kim,[†,‡,⊥] Tae Hoon Lee,[§,⊥] Elton J. G. Santos,[†,#,^] Pil Sung Jo,[∥] Alberto Salleo,[∥] Yoshio Nishi,[§] and Zhenan Bao[*,†]

[†]Department of Chemical Engineering, [§]Department of Electrical Engineering, and [∥]Department of Materials Science and Engineering, Stanford University, Stanford, California 94305, United States, [#]School of Mathematics and Physics, Queen's University Belfast, University Road, Belfast BT7 1NN, United Kingdom, [^]School of Chemistry and Chemical Engineering, Queen's University Belfast, David Keir Building, Belfast BT9 5AL, United Kingdom, and [‡]Department of Physics, Ulsan National Institute of Science and Technology (UNIST), Ulsan 689-798, Korea. [⊥]K.K. and T.H.L. contributed equally to this work.

ABSTRACT Graphene, with its unique electronic and structural qualities, has become an important playground for studying adsorption and assembly of various materials including organic molecules. Moreover, organic/graphene vertical structures assembled by van der Waals interaction have potential for multifunctional device applications. Here, we investigate structural and electrical properties of vertical heterostructures composed of C_{60} thin film on graphene. The assembled film structure of C_{60} on graphene is investigated using transmission electron microscopy, which reveals a uniform morphology of C_{60} film on graphene with a grain size as large as 500 nm. The strong epitaxial relations between C_{60} crystal and graphene lattice directions are found, and van der Waals *ab initio* calculations support the observed phenomena. Moreover, using C_{60}–graphene heterostructures, we fabricate vertical graphene transistors incorporating n-type organic semiconducting materials with an on/off ratio above 3×10^3. Our work demonstrates that graphene can serve as an excellent substrate for assembly of molecules, and attained organic/graphene heterostructures have great potential for electronics applications.

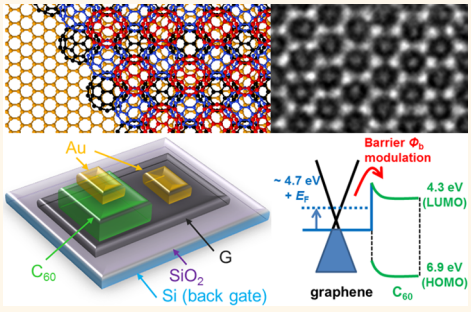

KEYWORDS: graphene · C_{60} · vertical transistors · organic semiconducting molecules · vertical heterostructures

Graphene-supported heterostructures open up possibilities for various interesting phenomena and applications.[1] Recently, layered heterostructures using graphene and inorganic 2D materials assembled by van der Waals (vdW) interaction (or mechanical transfer/stacking) have become interesting device platforms.[2] Especially, inorganic layered materials such as MoS_2 and WS_2 layers have been incorporated into heterostructures with graphene, and their electronic/optoelectrical properties have shown promising results.[3−5] Related epitaxial growth of inorganic materials on graphene has been also pursued.[6−8]

Assembly of organic materials on graphene has also generated broad interest,[9,10] and its potential for organic transistors and organic photovoltaics has been under investigation.[11−14] The organic molecules can be adsorbed onto graphene mainly by vdW interaction. The crystal structures adopted by organic molecules are governed by competition between molecule–molecule interactions and molecule–substrate interactions. Many applications involving organic materials have pursued optimal crystal structures by various methods.[15] In this aspect, graphene has recently emerged as an excellent template for fabricating well-ordered structures with atomic scale objects such as organic molecules and inorganic nanoparticles. Of high importance is the control of molecular packing on graphene and utilizing electrical properties of such assembly structures.

In this paper, we study C_{60}–graphene vertical heterostructures assembled by vdW interactions. Transmission electron microscopy (TEM) reveals the uniform C_{60} film morphology on graphene, and we find strong epitaxial relations between the C_{60} crystal and graphene lattice directions. The preferential growth of C_{60} crystals along graphene's zigzag and armchair directions is experimentally observed and theoretically accounted for using *ab initio*

* Address correspondence to zbao@stanford.edu.

Received for review January 26, 2015 and accepted May 31, 2015.

Published online June 01, 2015
10.1021/acsnano.5b00581

calculations employing vdW interactions. Moreover, with the C_{60}−graphene vertical junction, we demonstrate the operation of graphene vertical transistors showing n-type transport behavior. The energy barrier modulation at the C_{60}−graphene Schottky junction can be used to achieve a high on/off ratio greater than 3×10^3, which is difficult to obtain for conventional graphene transistors. Our work demonstrates that graphene can serve as an excellent substrate for understanding the epitaxial assembly of organic semiconductors as well as for organic/graphene heterostructure electronic device applications.

RESULTS AND DISCUSSION

We begin with a discussion of thin-film structures of C_{60} assembly on graphene. Using TEM, we investigate the detailed C_{60} film structure as well as epitaxial relations of assembled C_{60} crystals to the graphene lattice. Previous studies of C_{60} assembly on graphene (graphene on metallic substrate or graphite) have mainly utilized scanning tunneling microscopy (STM) or low-energy electron diffraction (LEED).[16−20] STM studies have elucidated some important structural and electrical properties such as formation of specific C_{60} molecular orientations and adsorption sites on graphene substrates at low temperature.[16−19] LEED has been also used to investigate C_{60} film structures.[20] Notably, LEED of C_{60} on graphite did not show a strong epitaxial behavior.[20] In our study, the C_{60} film is prepared on a suspended graphene. With its high electrical conductivity and mechanical strength, graphene can serve as a unique substrate for TEM investigation. TEM allows us to study the micrometer scale structures of assembled films as well as to image C_{60} molecules at atomic/molecular scales. Recent studies have demonstrated that even single atoms adsorbed on the graphene surface[21,22] as well as organic film can be imaged using various TEM techniques.[23] Moreover, without effects from the underlying substrate, we expect to observe intrinsic assembly behavior from the graphene−C_{60} interaction. For example, graphene grown on Ru substrates shows high corrugation due to the graphene/Ru interaction, and specific preferential adsorption sites of C_{60} were reported.[16,17]

C_{60} film is deposited on graphene TEM grids by a thermal evaporation process (see Methods section for details). Figure 1 shows TEM images of C_{60} thin film grown on graphene TEM grids. In Figure 1a, the schematic of C_{60} film grown on a graphene membrane is shown. The central circle region is the suspended graphene membrane where C_{60} is assembled directly on graphene, while C_{60} crystals are grown on amorphous carbon outside the circle. C_{60} film (10 nm thickness and substrate temperature of 120 °C) shows high uniformity on graphene (Figure 1b−d). An atomically flat graphene substrate allows uniform formation of C_{60} film. The C_{60} morphology on amorphous carbon shows distinct morphology, showing a dominant island growth mode (Figure 1b,c). A zoomed-in TEM image of C_{60} film on a graphene membrane clearly shows highly ordered C_{60} crystal structure (Figure 1d). Moreover, the atomic resolution TEM images of C_{60} on graphene show a well-organized hexagonal honeycomb lattice structure. The simulated TEM image shows good agreement with experimental observations, which confirms close-packed C_{60} crystal structures.

The epitaxial relation between the C_{60} crystal axis and graphene lattice direction is systematically investigated by electron diffraction as well as high-resolution TEM imaging. Figure 2a,b shows representative selective area electron diffraction of C_{60}/graphene specimens. In this case, the size of the electron beam illumination is ∼300 nm. The lowest-order diffraction peaks of the C_{60} film show a *d*-spacing of 8.7 Å, which is consistent with the previous results from close-packed C_{60} crystals.[24] We note that, at room temperature, C_{60} molecules are under rotational motions and attain the face-centered cubic molecular structure.[25] As the C_{60} diffraction signals in Figure 2a,b show single-crystal-like diffractions, this suggests that the grain size of C_{60} crystals is larger than 300 nm. Generally, the C_{60} grain size is in the range of 300−500 nm. More interestingly, we observe a strong epitaxial growth of C_{60} crystals on graphene. The histogram of rotational angle Θ (the angle between the C_{60} crystal facet and the graphene zigzag lattice direction, Figure 2c) shows that C_{60} crystals have a higher growth tendency along the zigzag (ZZ) or armchair (AC) directions of graphene lattices, as shown in Figure 2d.

To explain the observed epitaxial behavior of C_{60} on graphene, we perform first-principles *ab initio* simulations employing vdW interactions. First, we consider various C_{60} molecular orientations toward the graphene substrate and calculate its adsorption energy. Due to the large number of possible configurations, a computational screening of relevant relative orientations of C_{60} on graphene has been performed, which resulted in nine different interface geometries. The adsorption energies were also computed without vdW dispersion forces (see Figure S1 in Supporting Information), which remarkably show energy differences of 1 order of magnitude smaller than those calculated including vdW interactions. This strongly suggests that vdW interactions play a role in the stabilization of the interface. After we constructed the C_{60} crystal made of different molecular orientations at Θ = 0°, we calculated the crystal-direction-dependent adsorption energies as a function of the rotational angle Θ.

Our first-principle calculations show that AC and ZZ have local minima for adsorption energies at low (∼2−6°) and high (∼23.5−28°) angles Θ, with energy gained between 0 and 30° reaching values up to

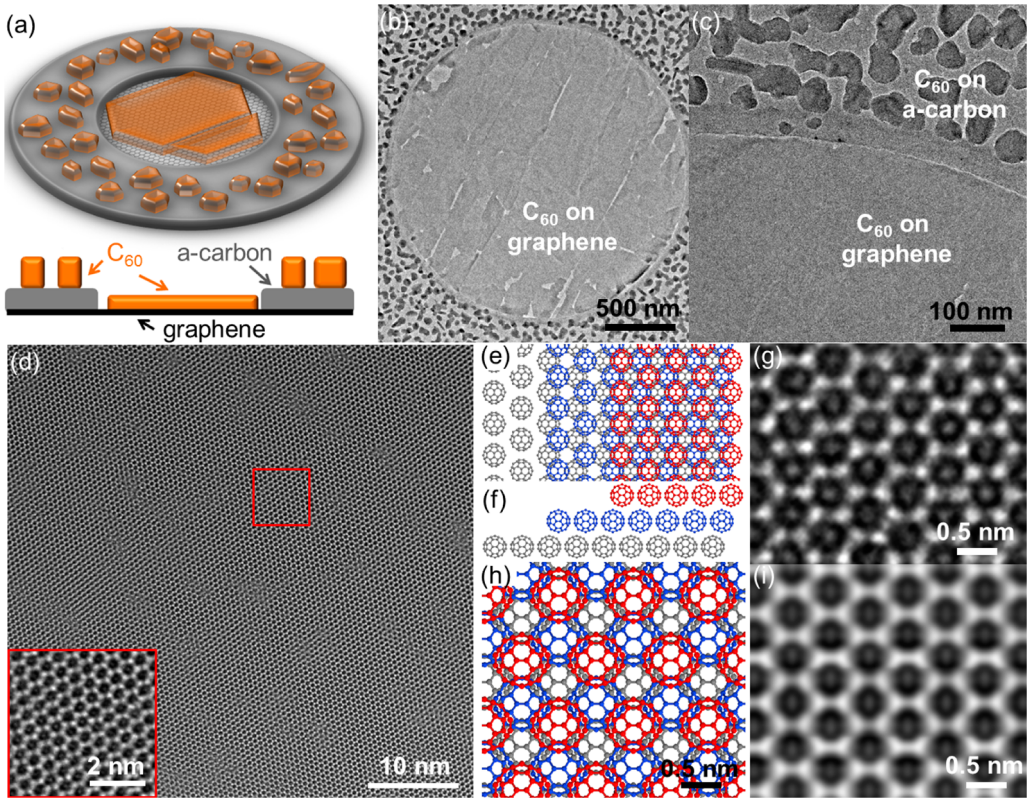

Figure 1. C_{60} thin film grown on graphene. (a) Schematic of C_{60} film grown on a graphene membrane. C_{60} is thermally evaporated to a graphene TEM grid. The central circular region has a suspended graphene membrane. Outside the circle, the C_{60} is evaporated onto an amorphous carbon film. Bottom image shows a side view of the sample geometry. (b) TEM image of C_{60} film (10 nm thickness) on graphene. C_{60} uniformly covers the graphene surface. (c) TEM image of C_{60} film around the edge of a hole in a Quantifoil TEM grid. The C_{60} morphology on amorphous carbon shows island growth. (d) Zoomed-in TEM image of C_{60} film on a graphene membrane. Uniform lattice structure of C_{60} is visible. Red square is a field of view for the inset. Inset clearly shows the crystal structure of the C_{60} thin film. (e) Schematic of the C_{60} crystal model with three C_{60} close-packed layers. The three layers (red, blue, and gray) of C_{60} have ABC stacking relation. (f) Side view of the C_{60} model shown in panel e. (g) Atomic resolution TEM image of a C_{60} crystal grown on graphene. (h) C_{60} crystal model with three layers. (i) TEM simulation image of model h.

−80 meV per C_{60} molecule at specific configurations (*e.g.*, pentagon/hole). Since C_{60} is under rotation and changes its relative configuration at room temperature,[25] a thermal ensemble of calculated energies with different configurations should be considered. On average, we still observe that low and high angles have local energy minima. This is in sound agreement with experimental observations shown in Figure 2d. The vdW simulations also show that most of the C_{60}/graphene interfaces change their energetic stability at different values of Θ once the systems assume new crystallographic orientations relative to the graphene surface. For instance, the pentagon/hole configuration is less stable than the apex-hole geometry (see Figure S1 in Supporting Information) at Θ = 0°, but at Θ = 30°, the former assumes higher stability than the latter. This suggests that the graphene axis along AC or ZZ directions could induce additional stability of the interfacial energy as a function of Θ. We note that a previous study on a similar system (C_{60} single-crystal graphite) shows a similar angular distribution with somewhat weak epitaxial effects.[20] We believe that the graphene TEM grid serves as an ideal substrate for C_{60} film formation, and their intrinsic C_{60}−graphene interaction (without substrate under graphene) can be observed in our system.

As we have demonstrated that graphene is an excellent substrate for C_{60} film formation, we now discuss device fabrications and electrical measurement of the C_{60}−graphene vertical junction. We prepare C_{60}−graphene junction devices on a SiO_2/Si substrate (Figure 3a). As graphene's work function (or Fermi level) is largely tunable due to its extremely small density of states at the Fermi level,[26] the interfacial energy barrier also can be effectively modulated by an external gate electric field (Figure 3b). This mechanism has been used for recent demonstration of vertical transistors and solar cells incorporating graphene.[3,5,27,28] The previous studies on graphene vertical transistors have mainly focused on inorganic/graphene heterostructures. On the other hand, the related study on organic/graphene counterparts has been limited,[13,29,30] especially for n-type organic materials,[31] although this platform has promising application potential for flexible electronics. As one of the high-performance n-type organic semiconductors,[32] C_{60}

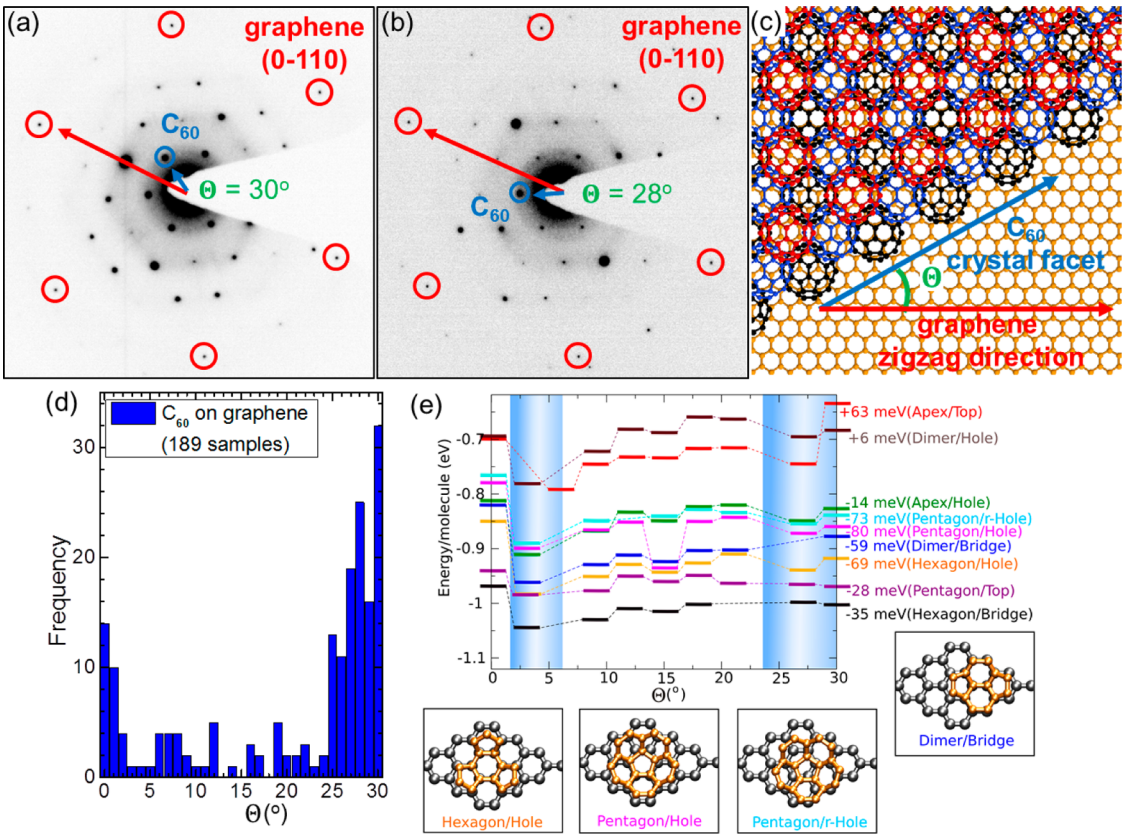

Figure 2. Epitaxial relation between the C_{60} molecular crystal and underlying graphene. (a,b) Selected area electron diffraction of C_{60} grown on graphene. The misorientation angle Θ is defined as an angle between the first-order diffraction signal of the C_{60} crystal and the first-order diffraction signal of the graphene lattice. (c) C_{60} crystal model on graphene. The misorientation angle Θ (as defined in panel a) can also be defined from an angle between the C_{60} crystal facet and the graphene zigzag lattice direction. (d) Histogram of experimentally observed misorientation angle Θ. The high angle (>25°) and very low angle (<2°) show high probability. (e) Misorientation angle Θ dependence of calculated adsorption energy of the C_{60} crystal on the graphene surface including van der Waals interactions with different adsorption configurations. The geometries used in the calculations with the highest energetic modifications as a function of Θ are shown as an inset labeled according to the color shown for each curve. The energy difference between adsorption energies at 0 and 30° are shown at the right side. Positive (negative) values correspond to a decrease (increase) of the energy stability for C_{60} on top of the graphene surface. The regions at low (~2−6°) and high (~23.5−28°) misorientation angles have local energy minima for various adsorption configurations and are highlighted in the shaded rectangles.

can be incorporated into graphene heterostructures to display n-type vertical transport behavior. For vertical device fabrications, various thicknesses (150−450 nm) of C_{60} are investigated, and the presented data are from 450 nm thickness unless otherwise noted.

Figure 3d shows a representative output curve of vertical junction devices. It shows nonlinear curves, and the current with positive V_{ds} shows high modulation with respect to V_g while the current modulation at negative V_{ds} is very small. The output curve with semilog scale shows that the junction shows quite an ideal diode behavior with an ideality factor η of approximately 1.9. As the lowest unoccupied molecular orbital (LUMO) and highest occupied molecular orbital (HOMO) of C_{60} are ~4.3 and ~6.9 eV,[33] the electrical transport occurs between the LUMO of C_{60} and the Fermi energy state of graphene (~4.7 eV). The high modulation at positive V_{ds} shows that the energy barrier for n-type transport is highly tunable, which is consistent with our energy band diagram (Figure 4a). The observed higher current with higher V_g is also consistent with our picture; Fermi energy level of graphene is raised with higher V_g, and the Schottky barrier is lowered accordingly, which results in higher current at the junction (Figure 4a). As displayed in Figure 3f, an on−off ratio greater than 3×10^3 is also demonstrated at V_{ds} = 2 V from optimized vertical devices. The on−off ratio is slightly lower at lower V_{ds}, but we still observe it around 10^3. This high on−off ratio is very difficult to achieve in conventional lateral graphene transistors. We note that it may be possible to achieve higher on/off ratios through perforated graphene electrodes and different dielectric materials, as recently demonstrated in vertical graphene organic transistors.[30,31]

To demonstrate that the Schottky barrier modulation at the junction is the main mechanism for current control, we measure the temperature-dependent vertical transport. The energy barriers with different gate voltages can be extracted from the relation,

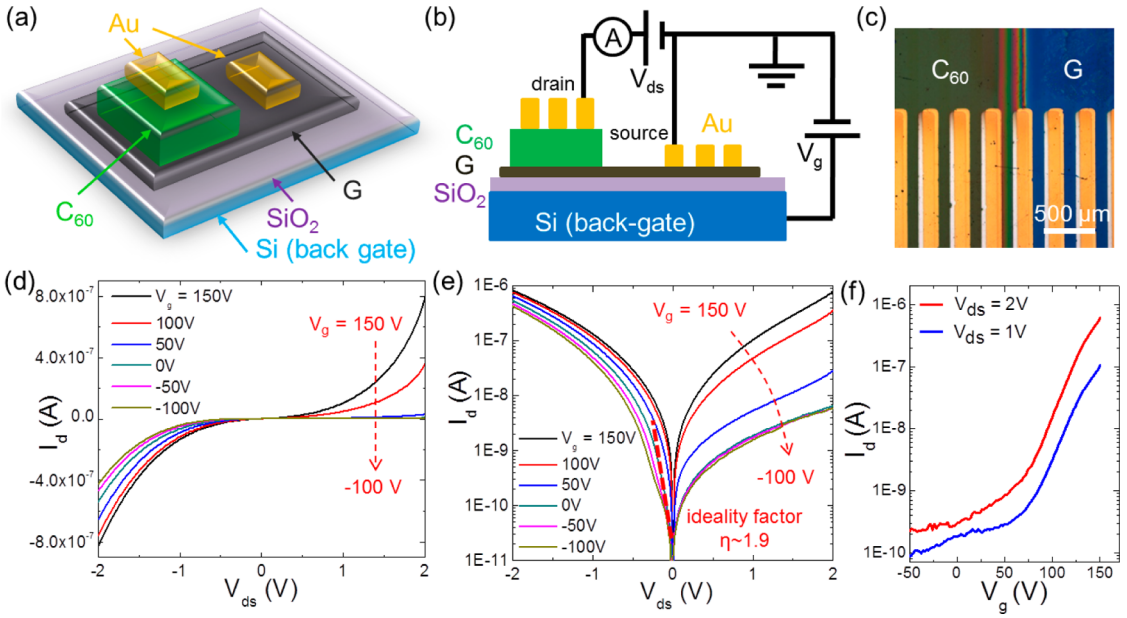

Figure 3. Vertical transport measurement of C_{60}−graphene vertical heterostructures. (a) Device geometry of C_{60}−graphene vertical structure. (b) Side view of the device geometry and measurement setup. (c) Optical image of a representative fabricated device. (d,e) Output curve (I_d−V_{ds}) with different applied gate voltages V_g. Panel e shows the current (*y*-axis) in log scale. (f) Representative transfer curves (I_d−V_g) of a device.

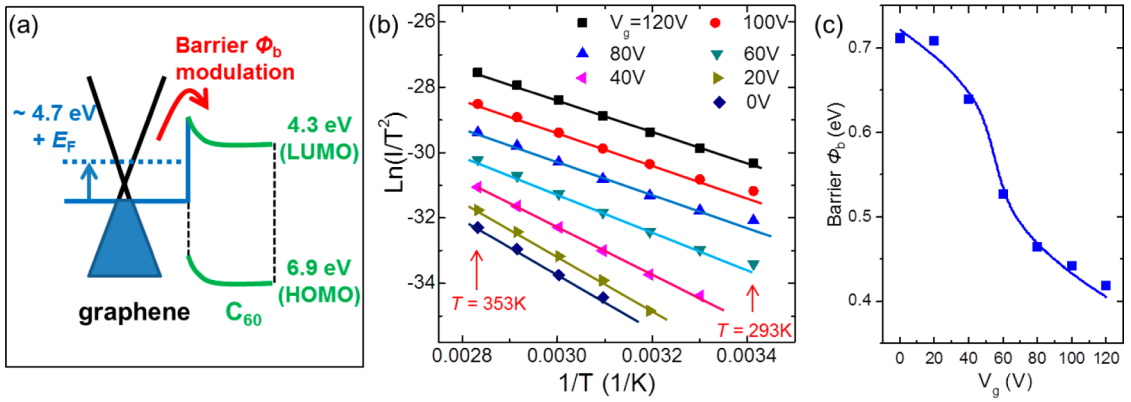

Figure 4. Measurements of C_{60}−graphene interface energy barriers. (a) Energy diagram of the graphene/C_{60} heterostructure. The Fermi energy of graphene is tunable with the gate electric field. The barrier at the C_{60}−graphene interface can be modulated according to the graphene Fermi energy shift. (b) Measurement of interface barrier energy by temperature-dependent vertical current measurement. The energy barriers with gate voltage modulation can be extracted from the slope (lines). (c) Value barrier ϕ_b as a function of electric field gating. The lines are derived from a model where the graphene work function change is estimated by charge density change induced by electric gating.

$\mathrm{Ln}(I/T^2) = -e\phi_b/k_BT$, where I is current, T is temperature, and ϕ_b is the energy barrier. Figure 4b shows data which are plotted in $\mathrm{Ln}(I/T^2)$ *versus* $1/T$. The devices show a linear dependence in the measured temperature ranges, and the change of slopes in Figure 4a shows that the obtained barrier is changed with different gate voltages. This confirms that the applied gate voltage can effectively tune the barrier energy.

In Figure 4c, we plot energy barriers corresponding to different gate voltages. The extracted energy barrier shows large modulations over 0.3 eV with different V_g. The vertical device with C_{60} shows steep variation of ϕ_b at $V_g \sim 50$ V (Figure 4c). This gate voltage corresponds to the Dirac point (minimum conduction point) V_D in a graphene device (Figure S2). We can estimate the Fermi energy shift of graphene by electric-field-induced gating. With graphene's band structure, the Fermi energy of graphene is given by $E_F = \mathrm{sign}(\Delta V_g)\hbar v_F(\alpha\pi|\Delta V_g|)^{1/2}$, where $\alpha = 7.1 \times 10^{10}$ cm^{-2} V^{-1} is the gate capacitance, $v_F = 1 \times 10^6$ ms^{-1} is the Fermi velocity of graphene, $\Delta V_g = V_g - V_D$ is the gate voltage difference from the Dirac point V_D. Ideally, the Fermi energy shift should be fully translated to energy barrier modulation, but we find that the modulation effect is somewhat smaller than what we expect. When we fit the measured data with the estimated Fermi energy shift by electric field gating, we find that the barrier modulation shows about 65% of expected Fermi energy

shift (line in Figure 4c) with a fitting parameter of V_D = 55 V. This can be attributed to a somewhat nonideal graphene−C_{60} interface and barrier pinning effect. The barrier modulation can be sensitive to the interfacial cleanness and other conditions.

CONCLUSION

We investigate the vertical structure composed of C_{60} and graphene. The well-ordered assembly of C_{60} molecules on graphene is studied using TEM. The n-type vertical transport through the C_{60}−graphene heterostructure shows a promising high on/off ratio with largely tunable energy barriers. Our study can be extended to other organic semiconductor systems. With its versatility, the organic/graphene heterostructure can be a very useful platform for electronics applications ranging from transistors to photovoltaics.

METHODS

Graphene Sample Preparation. Graphene was synthesized by chemical vapor deposition on 25 μm thick copper foil.[34] A graphene TEM sample was fabricated following a direct transfer method without using poly(methyl methacrylate) (PMMA) support.[35] Synthesized CVD graphene has an average of 5 μm grain size.[36] Graphene on the SiO_2/Si substrate was transferred using a PMMA support film.[34,37] PMMA solution was spin-coated on the surface of as-grown graphene on Cu foil at the speed of 2000 rpm for 1 min. The sample was left in air for 1 day to allow the solvent to evaporate thoroughly. O_2 plasma was then applied to remove the graphene layer on the other side of the Cu foil. The sample was placed into a solution of sodium persulfate ($Na_2S_2O_8$, a concentration of 0.1 g in 1 mL of water) to etch the underlying copper foil and was then rinsed with deionized water. The PMMA/graphene films were picked up by SiO_2/Si substrates and left for 24 h to obtain completely dry samples. The PMMA film was removed by soaking in acetone for 24 h and then rinsed with isopropyl alcohol and blown dry. Finally, sample annealing with a H_2 (20%) and Ar (80%) environment (with total pressure ~1 Torr) at 360 °C for 2 h was performed to remove residual PMMA and to obtain a cleaner graphene surface.

C_{60} Evaporation. C_{60} was evaporated using a thermal evaporator. For evaporation to TEM grids, a TEM grid was preannealed in air at 200 °C for 30 min to minimize the possible adsorbates on the graphene surface. After the preannealing process, TEM grids were attached onto the substrate with Kapton tape. The substrate temperature was held at 120 °C with an evaporation rate of 0.2 Å/s. C_{60} with a 10 nm thickness was prepared for TEM imaging. For device fabrication, a shadow mask with a 4 mm × 4 mm opening was used for C_{60} film deposition. The various substrate temperatures of 20−120 °C and the film thickness from 150 to 450 nm were investigated. The vacuum level was around 3×10^{-6} Torr during deposition.

Transmission Electron Microscopy. TEM imaging was performed with a FEI Titan operated at 80 kV equipped with an image corrector. Selective area electron diffraction was performed in a FEI Tecnai G2 F20 X-TWIN, operated at 200 kV. The TEM image simulations were performed using MacTempas and CrystalKit. The imaging acquisition conditions including a defocus value of 10 nm were used for the simulations of the C_{60} crystal.

Device Fabrication and Measurement. Au electrodes (80 nm thickness) were evaporated by a thermal evaporator using a shadow mask. The device measurement was performed inside a globebox using a Keithley 4200 parameter analyzer. For temperature-dependent data, device measurement was carried out in a vacuum probe station (MMR Technologies) at 10^{-4} mbar at a temperature range from 293 to 353 K.

Computational Details. Calculations were based on density functional theory using the SIESTA code.[38] The generalized gradient approximation[39] and nonlocal van der Waals density functional[40] were used together with a double-ζ plus polarized basis set, norm-conserving Troullier−Martins pseudopotentials,[41] and a mesh cutoff of 150 Ry. Atomic coordinates were allowed to relax using a conjugate gradient algorithm until all forces were smaller in magnitude than 0.01 eV/Å. Relevant lattice constants (in-plane and out-of-plane) were optimized for each system. To model the system studied in the experiments, we created large supercells containing up to 1692 atoms to simulate the interface between C_{60} and graphene layers. To avoid interactions between supercell images, the distance between periodic images of the C_{60}/graphene heterostructures along the direction perpendicular to the graphene plane was always larger than 20 Å. The resolution of the real-space grid used to calculate the Hartree and exchange-correlation contribution to the total energy was chosen to be equivalent to a 150 Ry plane-wave cutoff. The number of k-points was chosen according to the Monkhorst−Pack scheme[42] and was set to the equivalent of a 44 × 44 × 1 grid in the two-atom primitive unit cell of graphene, which gives well converged values for all of the calculated properties. We used a Fermi−Dirac distribution with an electronic temperature of k_BT = 21 meV.

Conflict of Interest: The authors declare no competing financial interest.

Supporting Information Available: Additional adsorption energy calculations of C_{60} on graphene with and without van der Waals interaction and representative data of graphene devices. The Supporting Information is available free of charge on the ACS Publications website at DOI: 10.1021/acsnano.5b00581.

Acknowledgment. Z.B. acknowledge support from National Science Foundation (Solid State Chemistry Program DMR-1303178). K.K. acknowledges support from Basic Science Research Program through the National Research Foundation of Korea (NRF) funded by the Ministry of Education (NRF-2014R1A1A2058178). E.J.G.S. acknowledges the use of computational resources provided by the Extreme Science and Engineering Discovery Environment (XSEDE), supported by NSF Grant Nos. TG-DMR120049 and TG-PHY120021. T.H.L. acknowledge the support from Toshiba Corporation through CIS-PMA program and a fellowship from ILJU foundation in South Korea.

REFERENCES AND NOTES

1. Georgakilas, V.; Otyepka, M.; Bourlinos, A. B.; Chandra, V.; Kim, N.; Kemp, K. C.; Hobza, P.; Zboril, R.; Kim, K. S. Functionalization of Graphene: Covalent and Non-covalent Approaches, Derivatives and Applications. *Chem. Rev.* **2012**, *112*, 6156–6214.
2. Geim, A. K.; Grigorieva, I. V. van der Waals Heterostructures. *Nature* **2013**, *499*, 419–425.
3. Britnell, L.; Gorbachev, R. V.; Jalil, R.; Belle, B. D.; Schedin, F.; Mishchenko, A.; Georgiou, T.; Katsnelson, M. I.; Eaves, L.; Morozov, S. V.; et al. Field-Effect Tunneling Transistor Based on Vertical Graphene Heterostructures. *Science* **2012**, *335*, 947–950.
4. Britnell, L.; Ribeiro, R. M.; Eckmann, A.; Jalil, R.; Belle, B. D.; Mishchenko, A.; Kim, Y. J.; Gorbachev, R. V.; Georgiou, T.; Morozov, S. V.; et al. Strong Light−Matter Interactions in Heterostructures of Atomically Thin Films. *Science* **2013**, *340*, 1311–1314.
5. Yang, H.; Heo, J.; Park, S.; Song, H. J.; Seo, D. H.; Byun, K.-E.; Kim, P.; Yoo, I.; Chung, H.-J.; Kim, K. Graphene Barristor, a Triode Device with a Gate-Controlled Schottky Barrier. *Science* **2012**, *336*, 1140–1143.

6. Shi, Y.; Zhou, W.; Lu, A.-Y.; Fang, W.; Lee, Y.-H.; Hsu, A. L.; Kim, S. M.; Kim, K. K.; Yang, H. Y.; Li, L.-J.; et al. van der Waals Epitaxy of MoS_2 Layers Using Graphene as Growth Templates. *Nano Lett.* **2012**, *12*, 2784–2791.
7. Hong, Y. J.; Lee, W. H.; Wu, Y.; Ruoff, R. S.; Fukui, T. van der Waals Epitaxy of InAs Nanowires Vertically Aligned on Single-Layer Graphene. *Nano Lett.* **2012**, *12*, 1431–1436.
8. Dang, W.; Peng, H.; Li, H.; Wang, P.; Liu, Z. Epitaxial Heterostructures of Ultrathin Topological Insulator Nanoplate and Graphene. *Nano Lett.* **2010**, *10*, 2870–2876.
9. MacLeod, J. M.; Rosei, F. Molecular Self-Assembly on Graphene. *Small* **2014**, *10*, 1038–1049.
10. Colson, J. W.; Woll, A. R.; Mukherjee, A.; Levendorf, M. P.; Spitler, E. L.; Shields, V. B.; Spencer, M. G.; Park, J.; Dichtel, W. R. Oriented 2D Covalent Organic Framework Thin Films on Single-Layer Graphene. *Science* **2011**, *332*, 228–231.
11. Lee, C.-H.; Schiros, T.; Santos, E. J. G.; Kim, B.; Yager, K. G.; Kang, S. J.; Lee, S.; Yu, J.; Watanabe, K.; Taniguchi, T.; et al. Epitaxial Growth of Molecular Crystals on van der Waals Substrates for High-Performance Organic Electronics. *Adv. Mater.* **2014**, *26*, 2812–2817.
12. Kang, S. J.; Lee, G.-H.; Yu, Y.-J.; Zhao, Y.; Kim, B.; Watanabe, K.; Taniguchi, T.; Hone, J.; Kim, P.; Nuckolls, C. Organic Field Effect Transistors Based on Graphene and Hexagonal Boron Nitride Heterostructures. *Adv. Funct. Mater.* **2014**, *24*, 5157–5163.
13. He, D.; Zhang, Y.; Wu, Q.; Xu, R.; Nan, H.; Liu, J.; Yao, J.; Wang, Z.; Yuan, S.; Li, Y.; et al. Two-Dimensional Quasi-Freestanding Molecular Crystals for High-Performance Organic Field-Effect Transistors. *Nat. Commun.* **2014**, *5*, 5162.
14. Zhang, Y.; Diao, Y.; Lee, H.; Mirabito, T. J.; Johnson, R. W.; Puodziukynaite, E.; John, J.; Carter, K. R.; Emrick, T.; Mannsfeld, S. C. B.; et al. Intrinsic and Extrinsic Parameters for Controlling the Growth of Organic Single-Crystalline Nanopillars in Photovoltaics. *Nano Lett.* **2014**, *14*, 5547–5554.
15. Li, H.; Giri, G.; Tok, J. B. H.; Bao, Z. Toward High-Mobility Organic Field-Effect Transistors: Control of Molecular Packing and Large-Area Fabrication of Single-Crystal-Based Devices. *MRS Bull.* **2013**, *38*, 34–42.
16. Li, G.; Zhou, H. T.; Pan, L. D.; Zhang, Y.; Mao, J. H.; Zou, Q.; Guo, H. M.; Wang, Y. L.; Du, S. X.; Gao, H.-J. Self-Assembly of C_{60} Monolayer on Epitaxially Grown, Nanostructured Graphene on Ru(0001) Surface. *Appl. Phys. Lett.* **2012**, *100*, 013304.
17. Lu, J.; Yeo, P. S. E.; Zheng, Y.; Yang, Z.; Bao, Q.; Gan, C. K.; Loh, K. P. Using the Graphene Moiré Pattern for the Trapping of C_{60} and Homoepitaxy of Graphene. *ACS Nano* **2012**, *6*, 944–950.
18. Cho, J.; Smerdon, J.; Gao, L.; Süzer, Ö.; Guest, J. R.; Guisinger, N. P. Structural and Electronic Decoupling of C_{60} from Epitaxial Graphene on SiC. *Nano Lett.* **2012**, *12*, 3018–3024.
19. Jung, M.; Shin, D.; Sohn, S.-D.; Kwon, S.-Y.; Park, N.; Shin, H.-J. Atomically Resolved Orientational Ordering of C_{60} Molecules on Epitaxial Graphene on Cu(111). *Nanoscale* **2014**, *6*, 11835–11840.
20. Shin, H.; O'Donnell, S. E.; Reinke, P.; Ferralis, N.; Schmid, A. K.; Li, H. I.; Novaco, A. D.; Bruch, L. W.; Diehl, R. D. Floating Two-Dimensional Solid Monolayer of C_{60} on Graphite. *Phys. Rev. B* **2010**, *82*, 235427.
21. Meyer, J. C.; Girit, C. O.; Crommie, M. F.; Zettl, A. Imaging and Dynamics of Light Atoms and Molecules on Graphene. *Nature* **2008**, *454*, 319–322.
22. Erni, R.; Rossell, M. D.; Nguyen, M.-T.; Blankenburg, S.; Passerone, D.; Hartel, P.; Alem, N.; Erickson, K.; Gannett, W.; Zettl, A. Stability and Dynamics of Small Molecules Trapped on Graphene. *Phys. Rev. B* **2010**, *82*, 165443.
23. Kim, K.; Santos, E. J. G.; Lee, T. H.; Nishi, Y.; Bao, Z. Epitaxially Grown Strained Pentacene Thin Film on Graphene. *Small* **2015**, *11*, 2037–2043.
24. Van Tendeloo, G.; Van Heurck, C.; Van Landuyt, J.; Amelinckx, S.; Verheijen, M. A.; Van Loosdrecht, P. H. M.; Meijer, G. Phase Transitions in Fullerene (C_{60}) and the Related Microstructure: A Study by Electron Diffraction and Electron Microscopy. *J. Phys. Chem.* **1992**, *96*, 7424–7430.
25. David, W. I. F.; Ibberson, R. M.; Dennis, T. J. S.; Hare, J. P.; Prassides, K. Structural Phase Transitions in the Fullerene C_{60}. *Europhys. Lett.* **1992**, *18*, 735.
26. Yu, Y.-J.; Zhao, Y.; Ryu, S.; Brus, L. E.; Kim, K. S.; Kim, P. Tuning the Graphene Work Function by Electric Field Effect. *Nano Lett.* **2009**, *9*, 3430–3434.
27. Vaziri, S.; Lupina, G.; Henkel, C.; Smith, A. D.; Östling, M.; Dabrowski, J.; Lippert, G.; Mehr, W.; Lemme, M. C. A Graphene-Based Hot Electron Transistor. *Nano Lett.* **2013**, *13*, 1435–1439.
28. Regan, W.; Byrnes, S.; Gannett, W.; Ergen, O.; Vazquez-Mena, O.; Wang, F.; Zettl, A. Screening-Engineered Field-Effect Solar Cells. *Nano Lett.* **2012**, *12*, 4300–4304.
29. Ojeda-Aristizabal, C.; Bao, W.; Fuhrer, M. S. Thin-Film Barristor: A Gate-Tunable Vertical Graphene-Pentacene Device. *Phys. Rev. B* **2013**, *88*, 035435.
30. Lemaitre, M. G.; Donoghue, E. P.; McCarthy, M. A.; Liu, B.; Tongay, S.; Gila, B.; Kumar, P.; Singh, R. K.; Appleton, B. R.; Rinzler, A. G. Improved Transfer of Graphene for Gated Schottky-Junction, Vertical, Organic, Field-Effect Transistors. *ACS Nano* **2012**, *6*, 9095–9102.
31. Hlaing, H.; Kim, C.-H.; Carta, F.; Nam, C.-Y.; Barton, R.; Petrone, N.; Hone, J.; Kymissis, I. Low-Voltage Organic Electronics Based on a Gate-Tunable Injection Barrier in Vertical Graphene-Organic Semiconductor Heterostructures. *Nano Lett.* **2015**, *15*, 69–74.
32. Li, H.; Tee, B. C. K.; Cha, J. J.; Cui, Y.; Chung, J. W.; Lee, S. Y.; Bao, Z. High-Mobility Field-Effect Transistors from Large-Area Solution-Grown Aligned C_{60} Single Crystals. *J. Am. Chem. Soc.* **2012**, *134*, 2760–2765.
33. Kang, S. J.; Yi, Y.; Kim, C. Y.; Cho, S. W.; Noh, M.; Jeong, K.; Whang, C. N. Energy Level Diagrams of C_{60}/Pentacene/Au and Pentacene/C_{60}/Au. *Synth. Met.* **2006**, *156*, 32–37.
34. Li, X. S.; Cai, W. W.; An, J. H.; Kim, S.; Nah, J.; Yang, D. X.; Piner, R.; Velamakanni, A.; Jung, I.; Tutuc, E.; et al. Large-Area Synthesis of High-Quality and Uniform Graphene Films on Copper Foils. *Science* **2009**, *324*, 1312–1314.
35. Regan, W.; Alem, N.; Aleman, B.; Geng, B. S.; Girit, C.; Maserati, L.; Wang, F.; Crommie, M.; Zettl, A. A Direct Transfer of Layer-Area Graphene. *Appl. Phys. Lett.* **2010**, *96*, 113102.
36. Kim, K.; Lee, Z.; Regan, W.; Kisielowski, C.; Crommie, M. F.; Zettl, A. Grain Boundary Mapping in Polycrystalline Graphene. *ACS Nano* **2011**, *5*, 2142–2146.
37. Reina, A.; Jia, X. T.; Ho, J.; Nezich, D.; Son, H. B.; Bulovic, V.; Dresselhaus, M. S.; Kong, J. Large Area, Few-Layer Graphene Films on Arbitrary Substrates by Chemical Vapor Deposition. *Nano Lett.* **2009**, *9*, 30–35.
38. Soler, J. M.; Artacho, E.; Gale, J. D.; Garcia, A.; Junquera, J.; Ordejon, P.; Sanchez-Portal, D. The Siesta Method for Ab Initio Order-*N* Materials Simulation. *J. Phys.: Condens. Matter* **2002**, *14*, 2745–2779.
39. Perdew, J. P.; Burke, K.; Ernzerhof, M. Generalized Gradient Approximation Made Simple. *Phys. Rev. Lett.* **1996**, *77*, 3865–3868.
40. Dion, M.; Rydberg, H.; Schröder, E.; Langreth, D. C.; Lundqvist, B. I. van der Waals Density Functional for General Geometries. *Phys. Rev. Lett.* **2004**, *92*, 246401.
41. Troullier, N.; Martins, J. L. Efficient Pseudopotentials for Plane-Wave Calculations. *Phys. Rev. B* **1991**, *43*, 1993–2006.
42. Monkhorst, H. J.; Pack, J. D. Special Points for Brillouin-Zone Integrations. *Phys. Rev. B* **1976**, *13*, 5188–5192.